Geophysical Journal International

Geophys. J. Int. (2020) **0,** 1–0
Advance Access publication 2020 October 17
GJI Gravity, Geodesy and Tides

doi: 10.1093/gji/ggaa500

GNSS characterization of hydrological loading in South and Southeast Asia

Kathryn Materna [1], Lujia Feng,[2] Eric O. Lindsey,[2] Emma M. Hill,[2,3] Aktarul Ahsan,[4] A.K.M. Khorshed Alam,[5] Kyaw Moe Oo,[6] Oo Than,[6] Thura Aung,[7] Saw Ngwe Khaing[8] and Roland Bürgmann[1,9]

[1] *Berkeley Seismology Laboratory, Berkeley, CA 94720, USA. E-mail: kmaterna@berkeley.edu*
[2] *Earth Observatory of Singapore, Nanyang Technological University, Singapore*
[3] *Asian School of the Environment, Nanyang Technological University, Singapore*
[4] *Geological Survey of Bangladesh, Bangladesh*
[5] *Formerly at Geological Survey of Bangladesh, Bangladesh*
[6] *Department of Meteorology and Hydrology, Myanmar*
[7] *Myanmar Earthquake Committee, Myanmar*
[8] *Department of Geology, Hinthada University, Hinthada, Myanmar*
[9] *UC Berkeley Earth and Planetary Science Department, University of California Berkeley, Berkeley, CA, USA*

Accepted 2020 October 13. Received 2020 October 11; in original form 2020 March 6

SUMMARY

The elastic response of the lithosphere to surface mass redistributions produces geodetically measurable deformation of the Earth. This deformation is especially pronounced in South and Southeast Asia, where the annual monsoon produces large-amplitude hydrological loads. The Myanmar–India–Bangladesh–Bhutan (MIBB) network of about 20 continuously operating Global Navigation Satellite Systems (GNSS) stations, established in 2011, provides an opportunity to study the Earth's response to these loads. In this study, we use GRACE temporal gravity products as an estimate of long-wavelength surface water distribution and use this estimate in an elastic loading calculation. We compare the predicted vertical deformation from GRACE with that observed with GNSS. We find that elastic loading inferred from the GRACE gravity model is able to explain the phase and much of the peak-to-peak amplitude (typically 2–3 cm) of the vertical GNSS oscillations, especially in northeast India and central Myanmar. GRACE-based corrections reduce the RMS scatter of the GNSS data by 30–45% in these regions. However, this approach does not capture all of the seasonal deformation in central Bangladesh and southern Myanmar. We show by a synthetic test that local hydrological effects may explain discrepancies between the GNSS and GRACE signals in these places. Two independent hydrological loading models of water stored in soil, vegetation, snow, lakes and streams display phase lags compared to the GRACE and GNSS observations, perhaps indicating that groundwater contributes to the observed loading in addition to near-surface hydrology. The results of our calculations have implications for survey-mode GNSS measurements, which make up the majority of geodetic measurements in this region. By using the GNSS data together with estimates of hydrological loading from independent observations and models, we may be able to more accurately determine crustal motions caused by tectonic processes in South and Southeast Asia, while also improving our ability to monitor the annual monsoon and resulting water storage changes in the region.

Key words: Loading of the Earth; Satellite geodesy; Time variable gravity.

1 INTRODUCTION

On seasonal timescales, hydrological cycles redistribute masses of water, ice and air around the globe. As these masses move, they impose gravitational loads on the solid Earth, and the Earth's de-

* Now at: Earthquake Science Center, US Geological Survey, Moffett Field, CA 94035, USA .

formation in response to the loads reveals information about both the sources of loading and the Earth itself (Blewitt *et al.* 2001). For example, loading deformation provides a means of understanding the exchange of mass between the atmosphere, surface water, soil moisture and groundwater (Argus *et al.* 2014, 2017; Milliner *et al.* 2018). With respect to the solid Earth, the surface response to time-varying loads also allows us to probe the elastic and viscoelastic structure of the crust and upper mantle (Chanard *et al.* 2018a). Furthermore, hydrological loads can be important sources of stress on faults, contributing to the timing and occurrence of earthquakes and non-volcanic tremor (Bettinelli *et al.* 2008; Pollitz *et al.* 2013; Craig *et al.* 2017; Johnson *et al.* 2017). For these applications as well as for the study of tectonic transients, it is valuable to understand the hydrological loading effects in geodetic data as accurately as possible.

For the study of tectonic processes, it is necessary to isolate deformation caused by mass loading from that caused by the earthquake cycle (e.g. Fu & Freymueller 2012). This can be a challenging task but is important in regions with transient earthquake cycle deformation and hydrological loads that vary from year to year. Accurate knowledge of hydrological loading in a region can also help with the interpretation of horizontal and vertical intermittent survey-mode GNSS measurements, which record the effects of both long-term tectonic deformation and hydrological loading but are sampled too sparsely in time to allow for their separation.

Hydrological processes generally produce millimetre-to-centimetre-level deformation of the Earth's surface through two dominant mechanisms. The first is elastic loading, in which the Earth's surface is deflected downward due to the weight of a load placed on or near the surface (Farrell 1972). The second mechanism is poroelastic loading, in which the addition of groundwater produces upward deflection by filling pore spaces and increasing fluid pressure within the rock below, and is often observed in aquifer settings (Galloway *et al.* 1999; Chaussard *et al.* 2015; Miller & Shirzaei 2015; Ojha *et al.* 2019). Both mechanisms primarily affect the vertical component of GNSS measurements, although they also act to a smaller degree on the horizontal components (Wahr *et al.* 2013; Silverii *et al.* 2016).

The typical methods used for studying hydrological loads in GNSS time-series involve applying either mathematical function fitting or hydrological models from independent data sets to assess the effects of elastic loading at GNSS stations. One of the most commonly used external models comes from the Gravity Recovery And Climate Experiment (GRACE) mission, which produces spatiotemporal descriptions of the Earth's gravity field and inferred redistribution of near-surface mass. A large body of research supports the general agreement between GRACE-based models of deformation and the hydrological loads observed in GNSS data (Tregoning *et al.* 2009; Fu & Freymueller 2012; Fu *et al.* 2013; Hao *et al.* 2016; Gu *et al.* 2017a; Chanard *et al.* 2018b; Yan *et al.* 2019; Saji *et al.* 2020). However, GRACE data products are relatively coarsely sampled in both space and time, having a spatial wavelength of 350–500 km and monthly sampling, and an inherent trade-off between temporal and spatial resolution in the processing. GRACE cannot capture local hydrological loading effects at individual GNSS stations, such as effects from large nearby streams or reservoirs, nor can it typically capture short-term temporal variations (Springer *et al.* 2019). Other types of information, such as water storage models derived from independent hydrological data sets, can be used to improve the spatial resolution of load sources near GNSS stations.

In this work, we seek to evaluate the performance of several techniques to model the seasonal deformation at GNSS stations in South and Southeast Asia (Fig. 1), an important tectonic region that also has a strong monsoon climate and large seasonal loading deformation (Steckler *et al.* 2010; Fu *et al.* 2013). We compute the average amplitude and phase of several loading models and compare them with the GNSS time-series and precipitation data. We assess how well the models reduce the variance of the GNSS data with the goal of separating the hydrological versus tectonic contributions to the deformation signal.

2 METHODS

2.1 GNSS data

We used data from the Myanmar–India–Bangladesh–Bhutan (MIBB) GNSS network operated by the Earth Observatory of Singapore (EOS) and their regional partners in each country in the network: the Department of Meteorology and Hydrology of Myanmar, the Myanmar Earthquake Committee, North Eastern Hill University in India, the Geological Survey of Bangladesh and Sherubtse College, Royal University of Bhutan. The network was first established in 2011. Most of the 24 stations began operation in 2012 and remain in operation, although some have significant data gaps. We used data until the summer of 2017, focusing on the period before the GRACE/GRACE-FO gap. We excluded 2 MIBB stations with less than 2 yr of data during this period. The list of excluded stations is shown in Table S1.

We processed the GNSS time-series using the GIPSY-OASIS software version 6.2 (Zumberge *et al.* 1997) following the processing strategy in Feng *et al.* (2015), with model corrections applied for solid Earth and pole tides and ocean tidal loading. We calculated ocean tidal loading relative to the centre of mass of the whole Earth including the solid Earth, oceans and atmosphere with the FES2004 model (Lyard *et al.* 2006), using the free ocean tidal loading calculator provided by the Onsala Space Observatory (http://holt.oso.chalmers.se/loading/). The coordinate time-series were produced in the International Terrestrial Reference Frame 2008 (ITRF2008, Altamimi *et al.* 2011) and subsequently rotated into a Sunda-fixed frame (Altamimi *et al.* 2012). The ITRF2008 reference frame is by definition a centre-of-mass frame, but in practice, it has been shown to more closely follow the Earth's centre-of-figure on seasonal and shorter timescales (Dong *et al.* 2003); this distinction is important for proper comparison with hydrological models in later sections. After processing the GNSS time-series, we then removed the effects of non-tidal atmospheric and non-tidal ocean loading using the 'NTAL' and 'NTOL' loading products provided by the Earth System Modelling group at the German Research Centre for Geosciences (GFZ, Dill & Dobslaw 2013) in the centre-of-figure frame. At two stations in central Myanmar (SDWN and SWBO), we also modelled and removed the signal related to the 2012 M_w 6.8 Thabeikkyin earthquake (Tun & Watkinson 2017) using Heaviside step functions for coseismic offsets and logarithmic functions for postseismic deformation (Feng *et al.* 2015). Where available, we also included 11 stations from a separate GNSS network in Bangladesh that was installed in 2007 as part of the NSF- and UNAVCO-supported BanglaPIRE project (Fig. 1, Steckler *et al.* 2010, 2016). Most of these stations have data from 2007 to 2011 (Fig. S4). These data are available from UNAVCO and were processed using the GIPSY-OASIS software with the same processing strategy as above.

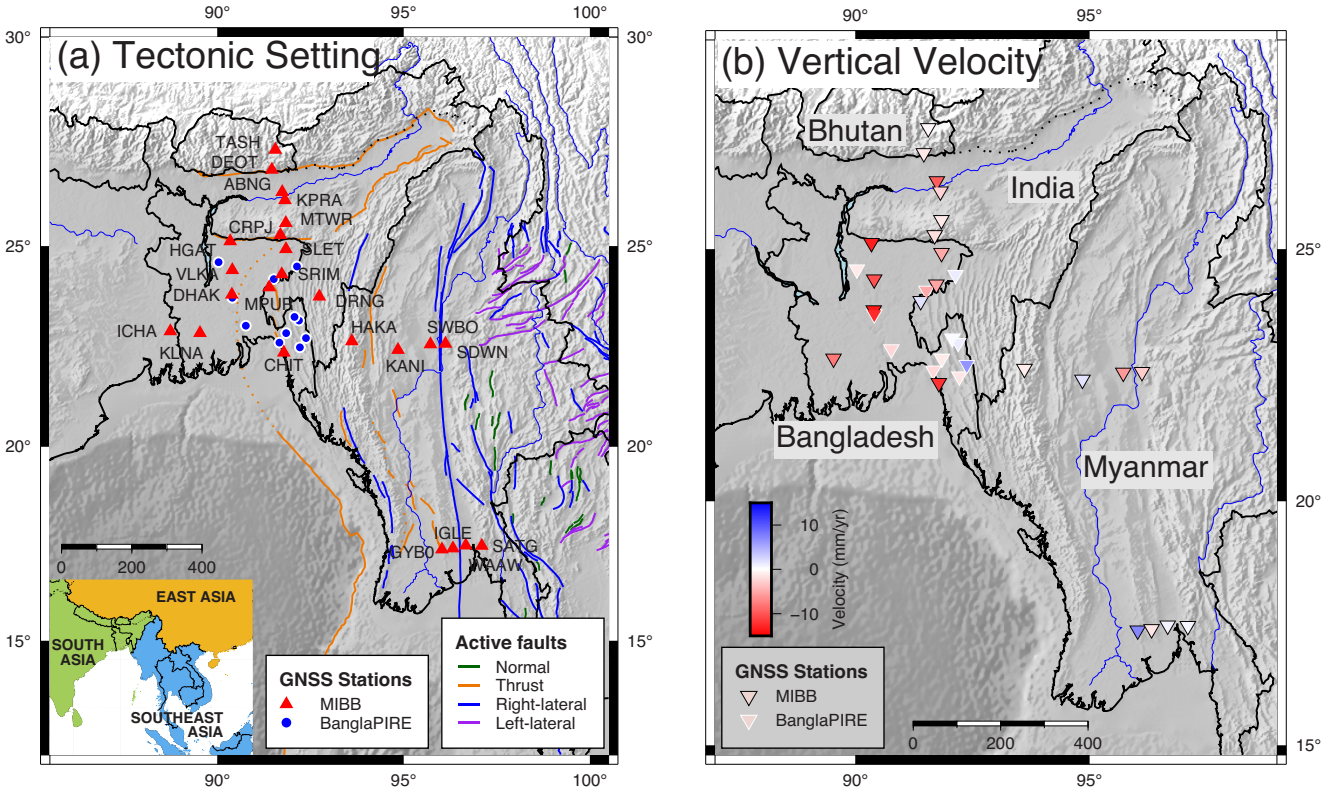

Figure 1. (a) Map of GNSS stations in South and Southeast Asia from two networks—the MIBB (Myanmar, India, Bangladesh and Bhutan) network and the BanglaPIRE network. Active faults are shown (Wang *et al.* 2014). (b) Vertical velocities of GNSS stations shown in (a), computed using least-squares fitting to the time-series.

2.2 Hydrological loading models

As the simplest model for yearly hydrological load cycles, we used a mathematical function to fit the average seasonal components in the GNSS time-series using least squares. In eq. (1), the coefficients *A*-*E* describe annual loading, semi-annual loading, and a constant velocity; *w* is the angular frequency associated with an annual period. This simple model is constrained to have constant-amplitude seasonal terms, so it cannot capture multi-annual hydrological variations.

$$x\ (t) = A\cos(wt) + B\sin(wt) + C\cos(2wt) + D\sin(2wt) + Et + F. \quad (1)$$

We then evaluated several physically based elastic loading models starting with a GRACE-gravity derived estimate of monthly surface mass changes. Our models are derived from the global Mascon gridded solution from NASA's Jet Propulsion Lab (JPL). GRACE Mascon data are available at http://grace.jpl.nasa.gov (Watkins *et al.* 2015; Wiese *et al.* 2016). The GRACE Level 2 data are corrected for ocean tidal loading, non-tidal ocean loading, and non-tidal atmospheric mass, meaning that contributions from those signals are not included in the product. We then computed the resulting elastic deformation at each GNSS station from all grid cells assuming a Preliminary Reference Earth Model (PREM) structure (Dziewonski & Anderson 1981, Fig. S1). We used loading Love numbers (Farrell 1972) for the loading Green's functions following the formulation of Fu & Freymueller (2012) and Johnson *et al.* (2020). The amplitude and phase of these models are estimated also using eq. (1).

In addition to GRACE, we considered several other elastic loading models from ground- and satellite-based hydrological products. The first of these is the Land Surface Discharge Model (LSDM), which models the elastic loading displacements driven by high-resolution hydrological models of terrestrial water storage and can be directly compared with geodetic time-series (Dill & Dobslaw 2013; Moreira *et al.* 2016). The LSDM estimates loads from shallow soil moisture, snow and surface water stored in rivers and lakes. The loading displacements are computed using an elastic 'ak135' Earth structure (Kennett Engdahl & Buland 1995). While ak135 is slightly different from PREM, these differences have been shown to produce only small changes (∼1 per cent change in amplitude reduction) in modelled hydrological loading (Wang *et al.* 2012; Gu *et al.* 2017b); furthermore, the differences in earth models are smallest in the vertical component that we study here (Wang *et al.* 2012). Hydrological loading displacement time-series for each coordinate were extracted from the LSDM website (last accessed on 7 July 2019) in the centre-of-figure frame.

We also considered loading driven by the Global Land Data Assimilation System (GLDAS) hydrological model (Rodell *et al.* 2004). This model contains $1^\circ \times 1^\circ$ monthly estimations of surface water in shallow soil moisture (upper 2 m), snow pack, and vegetation. Elastic loading deformation was computed on a PREM Earth structure following the technique of Wahr *et al.* (2013) and as implemented in North America for the Plate Boundary Observatory data set (Puskas Meertens & Phillips 2017). The summary of the three loading models (GRACE, LSDM and GLDAS) is presented in Table 1.

We assessed the performance of each of these models by evaluating the reduction in the weighted root mean square error (WRMS) of each detrended time-series before and after correction. The per cent improvement after correction shows the effectiveness of the

Table 1: Summary of data sets and products. Crosses indicate that the specific loading source is not included or considered in the model or that the loading source has been removed from the data through a separate model prior to its inclusion in this study. Checkmarks indicate that the loading source is included in the loading model or is expected to be present in the GNSS/GRACE data.

	GNSS	GRACE	LSDM	GLDAS
Ocean tidal	✗ (Corrected for)	✗ (Corrected for)	✗ (Not modelled)	✗ (Not modelled)
Ocean non-tidal	✗	✗	✗	✗
Atmosphere	✗	✗	✗	✗
Soil moisture	✓	✓	✓	✓
Snow	✓	✓	✓	✓
Vegetation	✓	✓	✗	✓
Lakes + Rivers	✓	✓	✓	✗
Groundwater	✓	✓	✗	✗
Resolution	–	350–500 km	0.125° × 0.125°	1° × 1°
Earth model	–	PREM	ak135	PREM

seasonal correction technique. Following van Dam *et al.* (2007), the WRMS reduction is calculated by:

$$\mathrm{WRMS}_{\mathrm{reduction}} = \frac{\mathrm{WRMS}_{\mathrm{GNSS}} - \mathrm{WRMS}_{\mathrm{GNSS-model}}}{\mathrm{WRMS}_{\mathrm{GNSS}}}. \quad (2)$$

For comparisons between GRACE-based loading models and vertical GNSS time-series, typical WRMS reductions around the globe and in South/Southeast Asia range from 20 to 50% (Fu & Freymueller 2012; Li *et al.* 2016; Saji *et al.* 2020), with higher being better. Understanding the differences between these time-series and increasing the WRMS reductions achieved by hydrological loading models (Chanard *et al.* 2018a) is an important aim of current research.

3 RESULTS

3.1 Least-squares results

When we fit the GNSS time-series with eq. (1), we find that GNSS stations across South and Southeast Asia record significant deformation at seasonal periods, generally in phase with the local hydrological cycle. Peak uplift is around April, at the end of the dry period, and peak subsidence is around October, at the end of the monsoon (Fig. S2). As shown in Fig. 2, the amplitudes of the vertical displacements are about 20 mm peak-to-peak. The amplitude and phase information of the seasonal oscillations in GNSS time-series is plotted more compactly in Fig. 3, where the phase and amplitude are combined into phasors (not physical vectors). The length of the phasor represents the peak-to-peak amplitude of the seasonal signal, and the phasor orientation represents the timing of peak uplift in the seasonal cycle as described by the legend.

3.2 Comparison with GRACE-derived load models

The GRACE mass loading model results are shown in Figs 3(a) and (b). Although the phases of the models are generally consistent with GNSS, the seasonal amplitudes of the GRACE models are systematically lower than the GNSS, especially in Myanmar. When the GRACE models are used to correct the GNSS time-series, the WRMS reduction is generally 20–45% (Fig. 3b). The oscillations from hydrological loading are visibly reduced in the time-series after the GRACE correction is applied (Figs S3 and S5). However, a few stations, typically those with misaligned phases between the GNSS and GRACE data, experience little WRMS reduction after seasonal correction by this technique (Fig. 3b). We assessed the GRACE model fit to the horizontal GNSS data as well but found the seasonal signals in the horizontal components are generally small and sometimes spatially incoherent (Fig. S7); more research into these horizontal seasonal oscillations is warranted in the future.

3.3 Comparison with LSDM and GLDAS hydrological load models

We find that the LSDM model predicts larger seasonal displacement patterns than the GRACE-derived model. The LSDM generally fits the amplitude of the GNSS seasonal oscillations very well across the network in South Asia. However, these models systematically reach peak uplift ∼1 month earlier than the GNSS. Because of the better match between the GNSS and LSDM seasonal amplitudes, the typical WRMS reduction for this model is slightly higher than for the GRACE corrections (Fig. 3d).

The GLDAS results are similar in phase to the LSDM, and similar in seasonal amplitude to the GRACE models. As a result, they disagree with the GNSS data by displaying lower amplitudes and phases that are ∼1 month too early. Correcting the GNSS data using this model is less effective than the other two methods, generally resulting in only 10–25% WRMS reductions (Fig. 3f).

Overall, we find that the GRACE-derived and LSDM-derived hydrological loading models capture the majority of seasonal signals in the vertical GNSS time-series, although in slightly different ways. We find that GRACE models best match the phase of the observed data, suggesting that the gravity data successfully capture the overall temporal pattern of seasonal mass loading experienced at most stations. On the other hand, the LSDM-based models best match the GNSS seasonal amplitudes. LSDM seems to provide a similar phase estimate but larger seasonal amplitude estimate compared to GLDAS.

We analyse these results geographically in Fig. 4 by showing WRMS reduction at each station partitioned by region. The WRMS reductions from GRACE, LSDM and GLDAS are shown as red triangles, blue squares and green circles, respectively. We find that GRACE models generally have the highest WRMS reduction in the upland or mountainous parts of the study region, including the Indoburman Range, the Shillong Plateau, Bhutan and the foreland of the Indian Himalaya (Fig. 4). However, the LSDM is the model with the highest WRMS reduction in India/Bangladesh and in the southern part of Myanmar.

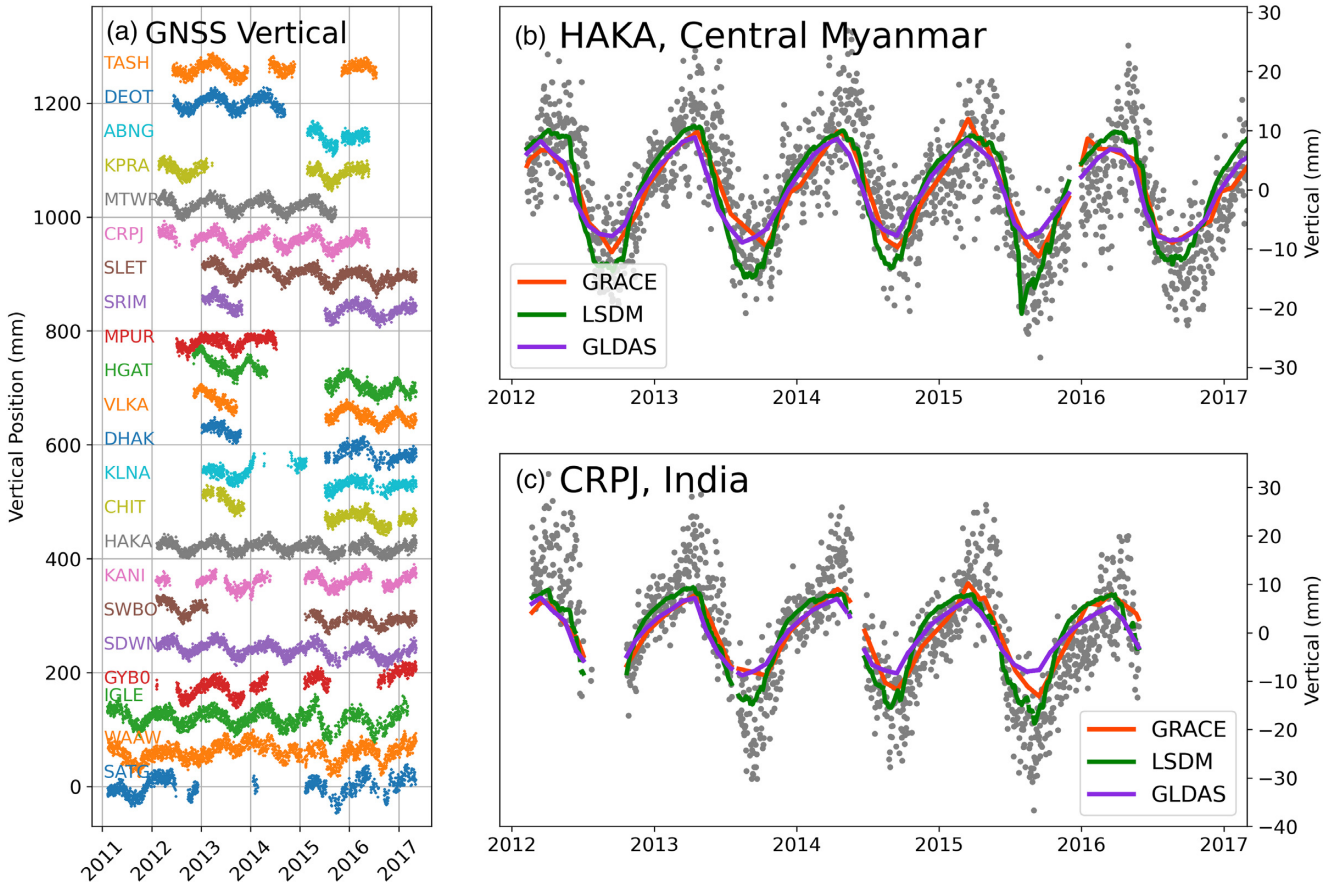

Figure 2. (a) GNSS vertical time-series from the MIBB network spanning from 2012 to 2017. (b and c) Two stations' vertical time-series with their corresponding hydrological loading models.

4 DISCUSSION

The patterns in our estimates of seasonal loading phase and amplitude (both across data sets and across the region) may help illuminate the underlying physical processes evident in the vertical GNSS time-series. As one example, the GRACE models and the GNSS data have a systematic phase lag compared to the LSDM and GLDAS of about 15 d (Table 2). One hypothesis for this phase difference is the slow movement of water through the groundwater system; the loading due to groundwater should be visible in GRACE and GNSS but not in LSDM and GLDAS, contributing a phase lag. An order-of-magnitude calculation of diffusive groundwater transport using typical hydraulic diffusivities (Barbour & Wyatt 2014) shows that 15 d is too short a timescale for significant lateral groundwater flow to take place; however, it could account for the flow of surface water into unconfined aquifers, removing it from the surface-water-only models (LSDM and GLDAS) but not the mass-sensitive observations (GNSS and GRACE, Fig. S9). A similar phase lag (20 d in the same direction) was inferred between GRACE-based groundwater estimates and terrestrial water storage from hydrological models in India (Rodell *et al.* 2009). Further work to better understand the phase difference between these hydrological models and GNSS data should consider spatial heterogeneity in the size, depth and structure of aquifers.

The GRACE loading models in our study underpredict observed GNSS seasonal amplitudes at nearly all stations as shown in Fig. 5, an effect that has also been observed in other parts of the world (Tregoning *et al.* 2009; Fu *et al.* 2013; Zhao Wu & Wu 2017). Fu *et al.* (2013) suggested that scaling GRACE models by a factor of 1.22 was needed to match vertical GNSS data in South Asia, and we find comparable seasonal amplitude differences between GRACE models and GNSS data. Similarly, our GRACE amplitude predictions are systematically lower than LSDM, a surprising result given that LSDM should represent a subset of GRACE's total mass budget (i.e. only the water associated with rivers, lakes and shallow soil moisture). The same amplitude discrepancy was also found in Yunnan Province and several other regions of China (Yan *et al.* 2019). Earth model differences between these two models should not be able to explain the magnitude of the GRACE versus LSDM discrepancy, as PREM and ak135 produce similar vertical displacements for the same load distribution (Martens *et al.* 2016, their fig. 10; Wang *et al.* 2012, their table 2).

Through quantitative tests of loading distributions, we instead suggest that the reduced GRACE-modelled seasonal amplitudes are due in large part to unmodelled loading from local water sources below the measurement resolution of GRACE. In Fig. 6, we modelled loading from the same hypothetical total mass under both localized loads from rivers and lakes (similar to the LSDM resolution) and distributed loads (similar to the GRACE resolution). The distributed model (Fig. 6b) shows widespread 10–40% reductions in displacement across almost the entire region compared to the localized model (Fig. 6a), with very few stations experiencing increased loading amplitude as a result of the smoothing. Fig. 6(c) shows the differences between the two loading scenarios and shows that the largest discrepancies occur where local loading sources are expected to be dominant, such as near large rivers. This apparent

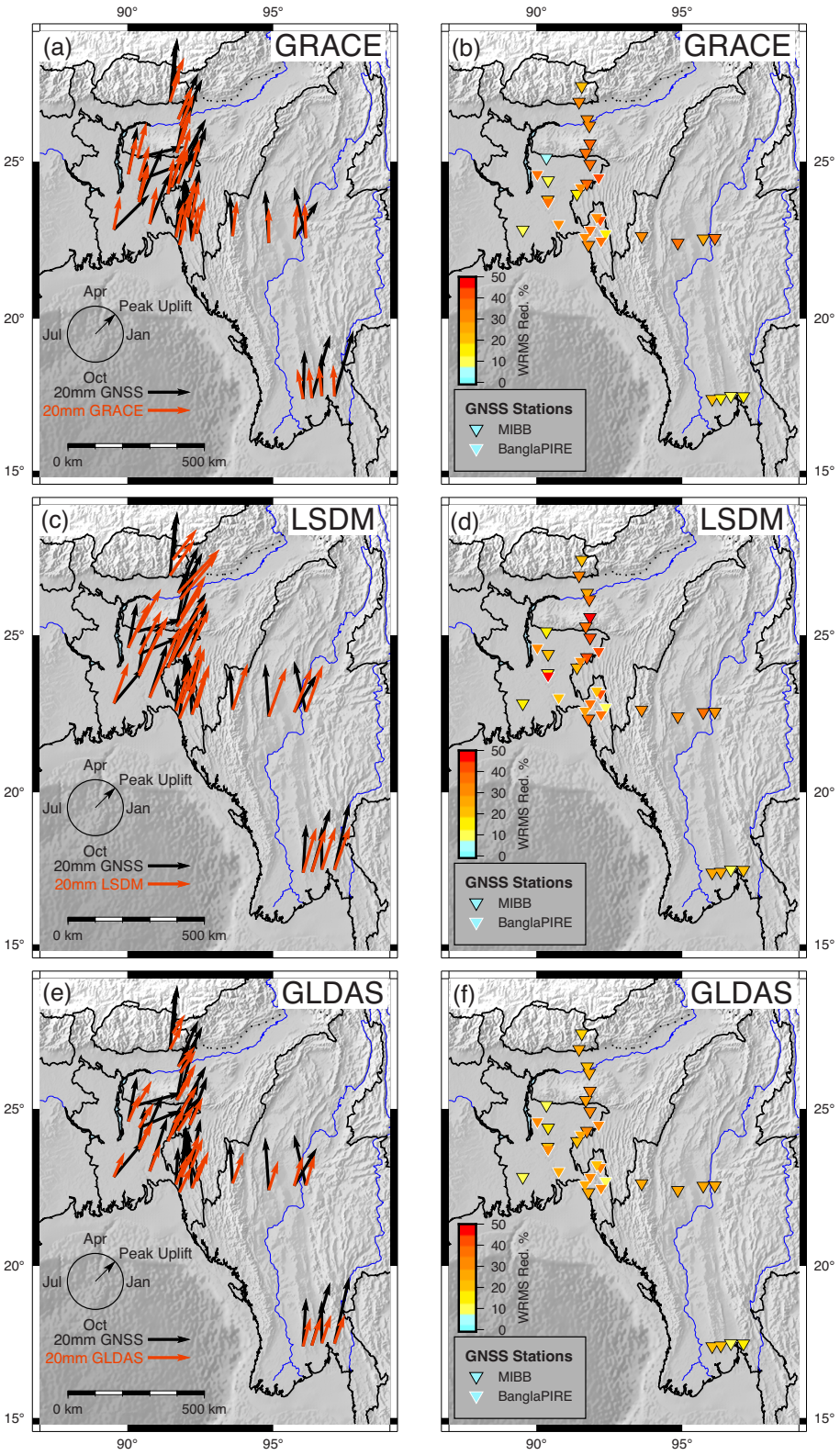

Figure 3. (a) Average phase and amplitude results for GNSS observations using a least-squares model fit (black) and GRACE models computed from the Mascon solution (red). The length of the vector shows the peak-to-peak amplitude of the seasonal oscillation and the angle shows the phase by denoting the timing of peak uplift as shown in the legend. (b) WRMS reduction (in per cent) between the uncorrected and corrected GNSS time-series using GRACE predicted displacements as corrections. (c and d) Phase and amplitude results for the LSDM, with its WRMS reduction. (e and f) Phase and amplitude results for the GLDAS model, with its WRMS reduction.

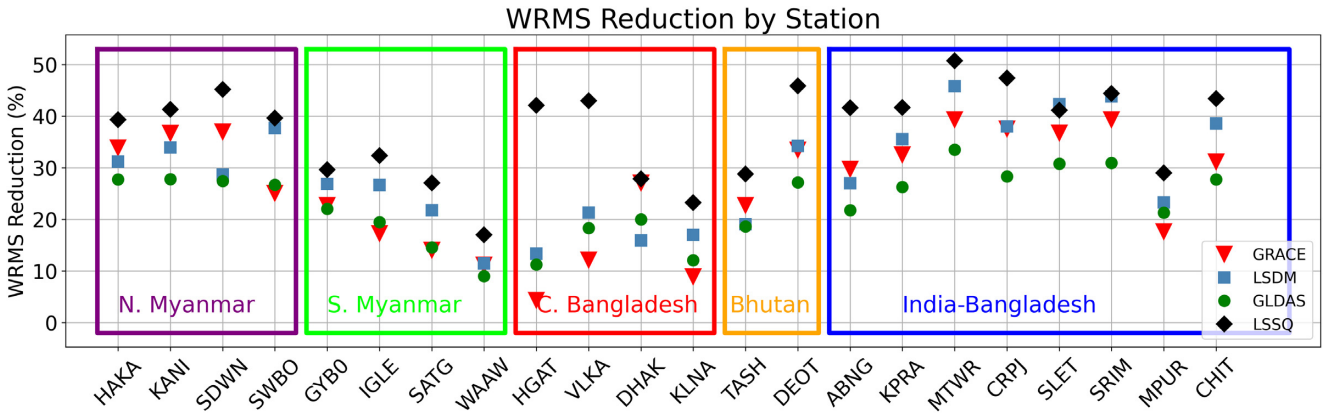

Figure 4. Station by station performance of each seasonal model. Higher WRMS reduction values indicate a stronger model fit. The LSSQ model is the reference model, derived from fitting eq. (1) to the GNSS time-series. Stations are grouped geographically and ordered north-to-south within groups where possible.

Table 2. Summary of seasonal deformation detected in the MIBB GNSS network (top row) and predicted by three hydrological model products. Their typical misfits and WRMS reductions with respect to the GNSS data are characterized in the three right-hand columns.

	Avg amplitude (mm)	Avg phase (DOY)	Avg amplitude misfit (mm)	Avg phase misfit (d)	Avg WRMS (per cent)
GNSS	23.3	74	-	-	-
GRACE	16.5	79	6.8	14.0 (mostly neg)	28.5
LSDM	22.9	65	3.5	17.4 (mostly pos)	29.7
GLDAS	13.8	65	9.5	17.3 (mostly pos)	24.3

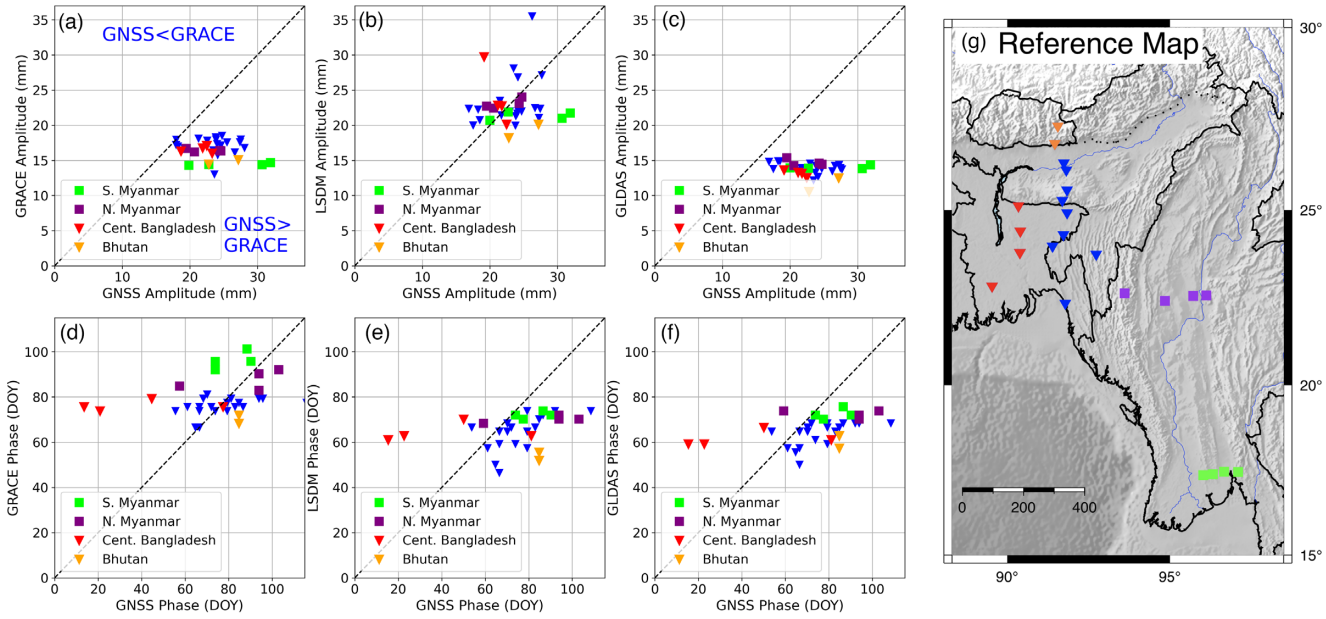

Figure 5. Comparisons of estimates of seasonal amplitude and phase from observed GNSS data and three models of hydrological loads. (a) GNSS amplitude versus GRACE model amplitude. (b) GNSS amplitude versus LSDM amplitude. (c) GNSS amplitude versus GLDAS model amplitude. (d–f) Comparisons of GNSS and model phase of peak uplift, in day of year. (b) Regional map with stations colour-coded for reference.

smoothing mechanism could explain the GRACE model's overall smaller seasonal displacements relative to the higher-resolution LSDM, as well as the modelled differences in the two largest deltas, the Ganges–Brahmaputra and Irrawaddy river deltas in Bangladesh and Myanmar (Fig. 4).

Specifically for GNSS stations located in sedimentary basins, Earth model effects from the shallow sedimentary layers may play a small secondary role in the discrepancy between the GNSS and GRACE amplitudes. The addition of a 5-km-thick surface layer of clay to PREM can result in a several-fold increase in loading response for loads on the order of several kilometres from the observation point (Bos 2010). However, because near-surface effects only amplify loads that are very close to GNSS stations (Martens *et al.* 2016), and because much of the seasonal amplitude of the

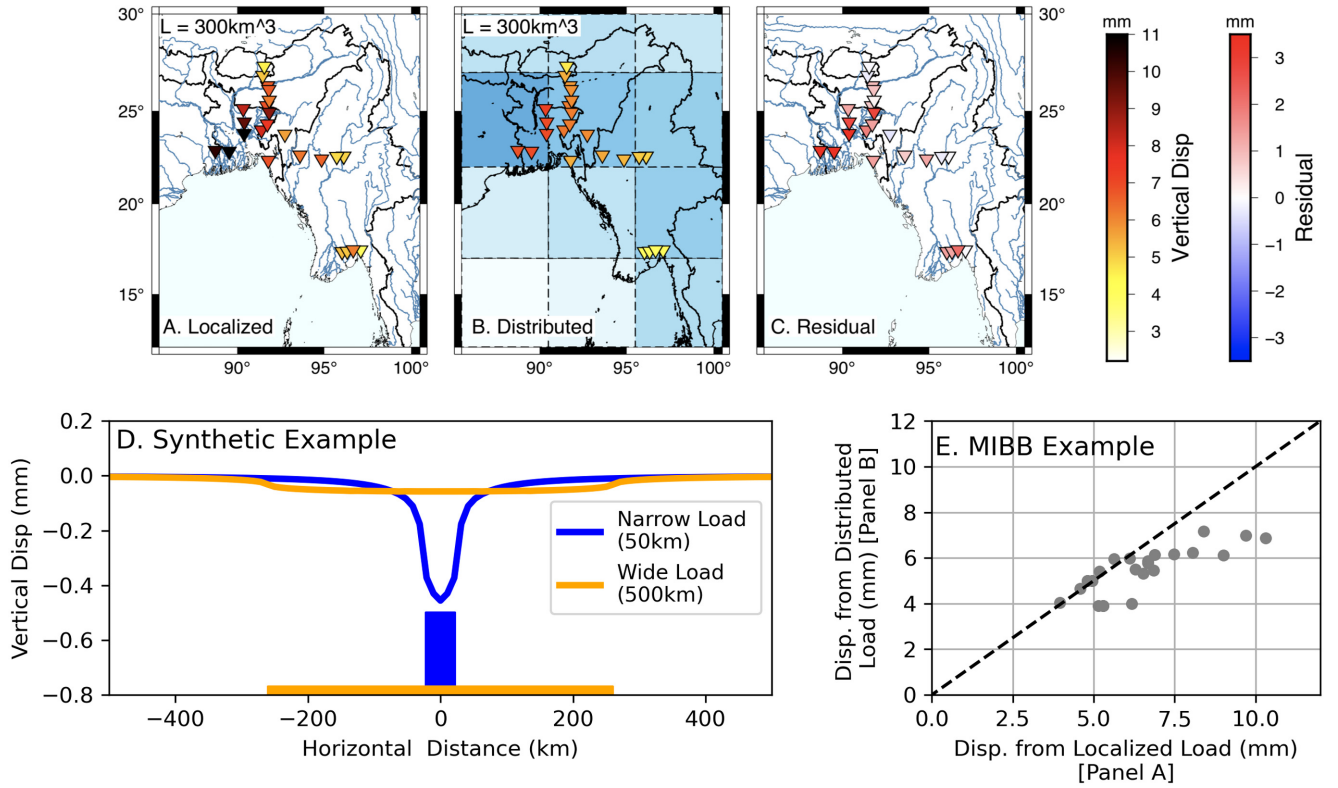

Figure 6. (a–c) Synthetic test of two identical-volume loads on the solid Earth, one locally distributed along rivers and lakes and one broadly distributed in large cells. The effect of local water bodies on the loading problem is shown by the residuals. Most stations have 10–40% higher loading amplitudes from localized loads compared to distributed loads of the same mass. (d) Example calculation from two equivalent-mass loads with different widths. (e) Residuals between panels (a) and (b).

GNSS data is already captured with the LSDM model, we consider these effects to be second-order at most stations. An even higher-resolution representation of loading from rivers, streams and lakes, perhaps focused on a particular subregion, could help quantify these approximations in the future.

We note that the phase and amplitude of hydrological loading signatures in GNSS time-series contain some inherent uncertainty and may include small contributions from other processes. For example, here we make the assumption that the phase and amplitude of seasonal deformation are consistent from year to year, but in reality, these vary slightly. In addition, estimation of the seasonal deformation is thought to depend somewhat on the GNSS processing. GNSS processing software and approaches may differ in their treatment of reference frame and Earth centre realization, draconitic errors and corrections for ocean tidal loading effects; these effects can impact both phase and amplitude of GNSS seasonal oscillations, but are usually much smaller than loading from the hydrological cycle (van Dam *et al.* 2016; Larochelle *et al.* 2018; Chanard *et al.* 2018a). Thermoelastic strains may contribute on the order of 1 mm to the GNSS-observed loading (Fang *et al.* 2014) but would not be included in hydrological models.

The results presented here can be used in a number of applications. In the future, a combined GNSS- and GRACE-derived estimate of total water storage would be higher resolution than a GRACE-based estimate alone (Fu *et al.* 2015; Adusumilli *et al.* 2019), and may provide new insights into the hydrological system in a monsoon region. An improved understanding of vertical seasonal and longer-term motion from elastic mass loading could also be used to extract more accurate tectonic velocity measurements from short time-series that contain a mix of hydrological loading effects and earthquake cycle deformation such as post-seismic transients. Model predictions of hydrological loading can be used to correct sparse time-series such as from survey-mode GNSS measurements (Zhao *et al.* 2017). Depending on the location of particular stations, we suggest that either GRACE or LSDM, or a combination of both, may provide the most accurate model from which to derive a hydrological correction for survey GNSS data. From a hazards perspective, it is important to have as precise a 3-D velocity field as possible in South and Southeast Asia, given that significant first-order questions still remain about the present-day activity of the Arakan megathrust and continental faults in the region (Steckler *et al.* 2016; Mallick *et al.* 2019). As more GNSS data are collected in Myanmar in the future, these corrections will help to further characterize tectonic activity in this complex plate boundary zone.

The study of vertical velocities from GNSS time-series is also an important research area that would benefit from accurate characterization of hydrological loads in Asia. Vertical velocities can reveal regions of elastic strain accumulation, active mountain-building, lower crustal flow, mantle upwelling, groundwater withdrawal, isostatic response to ice melt, sea level change and more (Hill et al., 2011; Serpelloni et al., 2013; Higgins *et al.* 2014; Hammond et al., 2016; Yi et al., 2016). In and around Myanmar, little is known about the processes affecting vertical deformation and the rheology of the crust. Separating the annual and multiannual hydrological signals from the existing GNSS data sets will provide insight into these questions by revealing regions where significant present-day vertical motion is attributable to tectonics.

5 CONCLUSIONS

In this work, we analyse continuous GNSS data from South and Southeast Asia to understand the patterns of hydrological loading deformation evident in their vertical time-series, which result in seasonal cycles of about 2–3 cm in amplitude. We then compare the observed loading signals to three hydrological modelling techniques to learn about the sources of loading on the solid Earth. We find that the best-fitting models derive from GRACE gravity data and a hydrological model (Dill & Dobslaw 2013) that contains estimates of water in soil moisture, snow and surface water. The loading component due to surface water in lakes and streams appears to be significant in this area, especially in the Ganges–Brahmaputra and Irrawaddy river deltas. At a larger scale, the comparison and integration of these data sets has the potential to provide insights into both the active tectonics and the spatiotemporal hydrological properties of South and Southeast Asia.

ACKNOWLEDGEMENTS

The authors thank the editor and two anonymous reviewers whose helpful comments greatly improved the manuscript. Many thanks to Christine Puskas at UNAVCO, who computed the GLDAS loading time-series. Thanks also to Yuning Fu for discussions and assistance. GRACE data are available at http://grace.jpl.nasa.gov as D. N. Wiese, D.-N. Yuan, C. Boening, F. W. Landerer, M. M. Watkins. 2018. JPL GRACE Mascon Ocean, Ice and Hydrology Equivalent Water Height Release 06 Coastal Resolution Improvement (CRI) Filtered Version 1.0. Ver. 1.0. PO.DAAC, CA, USA. Data set accessed [2020-05-02] at http://dx.doi.org/10.5067/TEMSC-3MJC6. Some figures were produced with the GMT software (Wessel *et al.* 2019). KM was supported by the National Science Foundation Graduate Research Fellowship Program and the EAPSI Singapore program. RB acknowledges support from award NNX17AE01G of the NASA Earth Surface and Interior program. The EOS authors and the installation and maintenance of the MIBB network were supported by the Earth Observatory of Singapore, the National Research Foundation of Singapore and the Singapore Ministry of Education under the Research Centres of Excellence initiative. EMH acknowledges support from a Singapore National Research Foundation Investigatorship award (NRF-NRFI05-2019-0009). The MIBB network is also supported by the staff of the EOS Center for Geohazards Observations and collaborators at the Department of Meteorology and Hydrology, Myanmar (Kyaw Moe Oo), Myanmar Earthquake Committee (U. Nyut Maung San), North Eastern Hill University (Devesh Walia), Geological Survey of Bangladesh (Aktarul Ahsan) and Sherubtse College, Royal University of Bhutan (Bimal Sharma). We also thank Syed Humayun Akhter at Dhaka University. This is EOS contribution number 308.

REFERENCES

Adusumilli, S., Borsa, A.A., Fish, M.A., McMillan, H.K. & Silverii, F., 2019. A decade of terrestrial water storage changes across the contiguous United States from GPS and GRACE, *Geophys. Res. Lett.,* **46** (22), 13 006–13 015.

Altamimi, Z., Collilieux, X. & Metivier, L., 2011. ITRF2008: an improved solution of the International Terrestrial Reference Frame, *J. Geod.,* **85**(8), 457–473.

Altamimi, Z., Metivier, L. & Collilieux, X., 2012. ITRF2008 plate motion model, *J. geophys. Res.,* **117**. doi:10.1029/2011JB008930.

Argus, D.F., Fu, Y. & Landerer, F.W., 2014. Seasonal variation in total water storage in California inferred from GPS observations of vertical land motion, *Geophys. Res. Lett.,* **41,** 1971–1980.

Argus, D.F., Landerer, F.W., Wiese, D.N., Martens, H.R., Fu, Y., Famiglietti, J.S. & Watkins, M.M., 2017. Sustained water loss in California's mountain ranges during severe drought from 2012 to 2015 inferred from GPS, *J. geophys. Res.,* **122**(12), 10 559–10 585.

Barbour, A.J. & Wyatt, F.K., 2014. Modeling strain and pore pressure associated with fluid extraction: the Pathfinder Ranch experiment, *J. geophys. Res.,* **119**(6), 5254–5273.

Bettinelli, P., Avouac, J.P., Flouzat, M., Bollinger, L., Ramillien, G., Rajaure, S. & Sapkota, S., 2008. Seasonal variations of seismicity and geodetic strain in the Himalaya induced by surface hydrology, *Earth planet. Sci. Lett.,* **266,** 332–344.

Blewitt, G., Lavalee, D., Clarke, P. & Nurutdinov, K., 2001. A new global mode of earth deformation: seasonal cycle detected, *Science,* **294,** 2342–2345.

Bos, M.S., 2010. Comment on "anomalous ocean load tide signal observed in lake-level variations in Tierra del Fuego" by A. Richter et al, *Geophys. Res. Lett.,* **37**(4), 1–2.

Chanard, K., Fleitout, L., Calais, E., Rebischung, P. & Avouac, J.P., 2018a. Toward a global horizontal and vertical elastic load deformation model derived from GRACE and GNSS station position time series, *J. geophys. Res.,* **123**(4), 3225–3237.

Chanard, K., Fleitout, L., Calais, E., Barbot, S. & Avouac, J.P., 2018b. Constraints on transient viscoelastic rheology of the asthenosphere from seasonal deformation, *Geophys. Res. Lett.,* **45**(5), 2328–2338.

Chaussard, E., Bürgmann, R., Shirzaei, M., Fielding, E.J. & Baker, B., 2015. Predictability of hydraulic head changes and characterization of aquifer-system and fault properties from InSAR-derived ground deformation, *J. geophys. Res.,* **119,** 6572–6590.

Craig, T.J., Chanard, K. & Calais, E., 2017. Hydrologically-driven crustal stresses and seismicity in the New Madrid Seismic Zone, *Nat. Commun.,* **8**(1). doi:10.1038/s41467-017-01696-w.

Dill, R. & Dobslaw, H., 2013. Numerical simulations of global-scale high-resolution hydrological crustal deformations, *J. geophys. Res.,* **118**(9), 5008–5017.

Dong, D., Yunck, T. & Heflin, M., 2003. Origin of the International Terrestrial Reference Frame, *J. geophys. Res.,* **108**(B4), 2200, doi:10.1029/2002jb002035.

Dziewonski, A.M. & Anderson, D., 1981. Preliminary reference Earth model, *Phys. Earth planet. Inter.,* **25**(4), 297–356.

Fang, M., Dong, D. & Hager, B.H., 2014. Displacements due to surface temperature variation on a uniform elastic sphere with its centre of mass stationary, *Geophys. J. Int.,* **196**(1), 194–203.

Farrell, W.E., 1972. Deformation of the Earth by surface loads, *Rev. Geophys.,* **10**(3), 761–797.

Feng, L., Hill, E.M., Banerjee, P., Hermawan, I., Tsang, L.L.H., Natawidjaja, D.H. & Sieh, K., 2015. A unified GPS-based earthquake catalog for the Sumatran plate boundary between 2002 and 2013, *J. geophys. Res.,* **120**(5), 3566–3598.

Fu, Y., Argus, D.F., Freymueller, J.T. & Heflin, M.B., 2013. Horizontal motion in elastic response to seasonal loading of rain water in the Amazon Basin and monsoon water in Southeast Asia observed by GPS and inferred from GRACE, *Geophys. Res. Lett.,* **40**(23), 6048–6053.

Fu, Y., Argus, D.F. & Landerer, F.W., 2015. GPS as an independent measure to estimate terrestrial water storage variations in Washington and Oregon, *J. geophys. Res.,* **120,** 552–566.

Fu, Y. & Freymueller, J.T., 2012. Seasonal and long-term vertical deformation in the Nepal Himalaya constrained by GPS and GRACE measurements, *J. geophys. Res.,* **117**(3), 1–14.

Galloway, D., Jones, D. & Ingebritsen, S.E., 1999, Land Subsidence in the United States, Report, USGS Numbered Series, Circular 1182, U.S. Geological Survey, doi:10.3133/cir1182.

Gu, Y., Fan, D. & You, W., 2017a. Comparison of observed and modeled seasonal crustal vertical displacements derived from multi-institution GPS and GRACE solutions, *Geophys. Res. Lett.,* **44**(14), 7219–7227.

Gu, Y., Yuan, L., Fan, D., You, W. & Su, Y., 2017b. Seasonal crustal vertical deformation induced by environmental mass loading in mainland China derived from GPS, GRACE and surface loading models, *Adv. Space Res.,* **59**(1), 88–102.

Hammond, W.C., Blewitt, G. & Kreemer, C., 2016. GPS imaging of vertical land motion in California and Nevada: implications for Sierra Nevada uplift, *J. geophys. Res.,* **121**(10), 7681–7703.

Hao, M., Freymueller, J.T., Wang, Q., Cui, D. & Qin, S., 2016. Vertical crustal movement around the southeastern Tibetan Plateau constrained by GPS and GRACE data, *Earth planet. Sci. Lett.,* **437,** 1–8.

Higgins, S.A., Overeem, I., Steckler, M.S., Syvitski, J.P.M., Seeber, L. & Akhter, S.H., 2014. InSAR measurements of compaction and subsidence in the Ganges-Brahmaputra Delta, Bangladesh, *J. geophys. Res.,* **119,** 1768–1781.

Hill, E.M., Davis, J.L., Tamisiea, M.E., Ponte, R.M. & Vinogradova, N.T., 2011. Using a spatially realistic load model to assess impacts of Alaskan glacier ice loss on sea level, *J. geophys. Res.,* **116**(10), 1–9.

Johnson, C.W., Fu, Y. & Bürgmann, R., 2017. Seasonal water storage, stress modulation, and California seismicity, *Science,* **356**(6343), 1161–1164.

Johnson, C.W., Fu, Y. & Burgmann, R., 2020. Hydrospheric modulation of stress and seismicity on shallow faults in southern Alaska, *Earth planet. Sci. Lett.,* **530,** 115904.

Kennett, B.L.N., Engdahl, E.R. & Buland, R., 1995. Constraints on seismic velocities in the Earth from traveltimes, *Geophys. J. Int.,* **122,** 108–124.

Larochelle, S., Gualandi, A., Chanard, K. & Avouac, J.P., 2018. Identification and extraction of seasonal geodetic signals due to surface load variations, *J. geophys. Res.,* **123**(12), 11 031–11 047.

Li, W., van Dam, T., Li, Z. & Shen, Y., 2016. Annual variation detected by GPS, GRACE and loading models, *Stud. Geophys. Geod.,* **60**(4), 608–621.

Lyard, F., Lefevre, F., Letellier, T. & Francis, O., 2006. Modelling the global ocean tides: modern insights from FES2004, *Ocean Dyn.,* **56,** 394–415.

Mallick, R., Lindsey, E.O., Feng, L., Hubbard, J., Banerjee, P. & Hill, E.M., 2019. Active convergence of the India-Burma-Sunda plates revealed by a new continuous GPS network, *J. geophys. Res.,* **124**(3), 3155–3171.

Martens, H.R., Rivera, L., Simons, M. & Ito, T., 2016. The sensitivity of surface mass loading displacement response to perturbations in the elastic structure of the crust and mantle, *J. geophys. Res.,* **121**(5), 3911–3938.

Miller, M.M. & Shirzaei, M., 2015. Spatiotemporal characterization of land subsidence and uplift in Phoenix using InSAR time series and wavelet transforms, *J. geophys. Res.,* **120,** 5822–5842.

Milliner, C., Materna, K., Bürgmann, R., Fu, Y., Moore, A.W., Bekaert, D. & Argus, D.F., 2018. Tracking the weight of Hurricane Harvey's stormwater using GPS data, *Sci. Adv.,* **4**(9). doi:10.1126/sciadv.aau2477.

Moreira, D.M., Calmant, S., Perosanz, F., Xavier, L., Filho, O.C.R., Seyler, F. & Monteiro, A.C., 2016. Comparisons of observed and modeled elastic responses to hydrological loading in the Amazon basin, *Geophys. Res. Lett.,* **43**(18), 9604–9610.

Ojha, C., Werth, S. & Shirzaei, M., 2019. Groundwater loss and aquifer system compaction in San Joaquin Valley During 2012–2015 Drought, *J. geophys. Res.,* **124**(3), 3127–3143.

Pollitz, F.F., Wech, A., Kao, H. & Bürgmann, R., 2013. Annual modulation of non-volcanic tremor in northern Cascadia, *J. geophys. Res.,* **118**(5), 2445–2459.

Puskas, C.M., Meertens, C.M. & Phillips, D., 2017. Hydrologic loading model displacements from the national and global data assimilation systems (NLDAS and GLDAS), Retrieved from https://www.unavco.org/data/gps-gnss/associated-products/hydrological/displacement-model-readme.pdf.

Rodell, B.Y.M., Houser, P.R., Jambor, U., Gottschalck, J., Mitchell, K., Meng, C. & Toll, D., 2004. The Global Land Data assimilation system this powerful new land surface modeling system integrates data from advanced observing systems to support improved forecast model initialization and hydrometeorological investigations, *Bull. Am. Meteorol. Soc.,* **85**(3), 381–394.

Rodell, M., Velicogna, I. & Famiglietti, J.S., 2009. Satellite-based estimates of groundwater depletion in India, *Nature,* **460**(7258), 999–1002.

Saji, A.P., Sunil, P.S., Sreejith, K.M., Gautam, P.K., Kumar, K.V., Ponraj, M. & Ramesh, D.S., 2020. Surface deformation and influence of hydrological mass over Himalaya and North India revealed from a decade of continuous GPS and GRACE observations, *J. geophys. Res.,* **125,** 1–17.

Serpelloni, E., Faccenna, C., Spada, G., Dong, D. & Williams, S.D.P., 2013. Vertical GPS ground motion rates in the Euro-Mediterranean region: New evidence of velocity gradients at different spatial scales along the Nubia-Eurasia plate boundary, *J. geophys. Res.,* **118**(11), 6003–6024.

Silverii, F., D'Agostino, N., Métois, M., Fiorillo, F. & Ventafridda, G., 2016. Transient deformation of karst aquifers due to seasonal and multiyear groundwater variations observed by GPS in southern Apennines (Italy), *J. geophys. Res.,* **121**(11), 8315–8337.

Springer, A., Karegar, M.A., Kusche, J., Keune, J., Kurtz, W. & Kollet, S., 2019. Evidence of daily hydrological loading in GPS time series over Europe, *J. Geod.,* **93,** 2145–2153.

Steckler, M.S., Mondal, D.R., Akhter, S.H., Seeber, L., Feng, L., Gale, J. & Howe, M., 2016. Locked and loading megathrust linked to active subduction beneath the Indo-Burman Ranges, *Nat. Geosci.,* **9**(8), 615–618.

Steckler, M.S., Nooner, S.L., Akhter, S.H., Chowdhury, S.K., Bettadpur, S., Seeber, L. & Kogan, M.G., 2010. Modeling earth deformation from monsoonal flooding in Bangladesh using hydrographic, GPS, and gravity recovery and climate experiment (GRACE) data, *J. geophys. Res.,* **115**(8), 1–18.

Tregoning, P., Watson, C., Ramillien, G., McQueen, H. & Zhang, J., 2009. Detecting hydrologic deformation using GRACE and GPS, *Geophys. Res. Lett.,* **36**(15), 1–6.

Tun, S.T. & Watkinson, I.M., 2017. Chapter 19 The Sagaing Fault, Myanmar, *Geol. Soc., Lond., Memoirs,* **48**(1), 413–441.

Van Dam, T., Ray, J., Sheehan, A., Herring, T.A., Murray, M.H. & Blewitt, G., 2016. Interpreting the GNSS vertical coordinate variations, in *American Geophysical Union Fall Meeting* (p. abstract #G13C03). San Francisco, CA.

van Dam, T., Wahr, J. & Lavallée, D., 2007. A comparison of annual vertical crustal displacements from GPS and Gravity Recovery and Climate Experiment (GRACE) over Europe, *J. geophys. Res.,* **112**(3), 1–11.

Wahr, J., Khan, S.A., Van Dam, T., Liu, L., Van Angelen, J.H., Van Den Broeke, M.R. & Meertens, C.M., 2013. The use of GPS horizontals for loading studies, with applications to northern California and southeast Greenland, *J. geophys. Res.,* **118**(4), 1795–1806.

Wang, H., Xiang, L., Jia, L., Jiang, L., Wang, Z., Hu, B. & Gao, P., 2012. Load Love numbers and Green's functions for elastic Earth models PREM, iasp91, ak135, and modified models with refined crustal structure from Crust 2.0, *Comp. Geosci.,* **49,** 190–199.

Wang, Y., Sieh, K., Tun, S.T., Lai, K.-Y. & Myint, T., 2014. Active tectonics and earthquake potential of the Myanmar region, *J. geophys. Res.,* **119,** 3767–3822.

Watkins, M.M., Wiese, D.N., Yuan, D.-N., Boening, C. & Landerer, F.W., 2015. Improved methods for observing Earth's time variable mass distribution with GRACE using spherical cap mascons, *J. geophys. Res.,* **120**(4), 2648–2671.

Wessel, P., Luis, J.F., Uieda, L., Scharroo, R., Wobbe, F., Smith, W.H.F. & Tian, D., 2019. The Generic Mapping Tools Version 6, *Geochem. Geophys. Geosyst.,* **20**(11), 5556–5564.

Wiese, D.N., Landerer, F.W. & Watkins, M.M., 2016. Quantifying and reducing leakage errors in the JPL RL05M GRACE mascon solution, *Water Resour. Res.,* **52,** 7490–7502.

Yan, J., Dong, D., Bürgmann, R., Materna, K., Tan, W., Peng, Y. & Chen, J., 2019. Separation of sources of seasonal uplift in China using independent component analysis of GNSS time series, *J. geophys. Res.,* **124,** 11, 11 951–11 971.

Yi, S., Freymueller, J.T. & Sun, W., 2016. How fast is the middle-lower crust flowing in eastern Tibet?, *J. geophys. Res.,* **121,** 6903–6915.

Zhao, Q., Wu, W. & Wu, Y., 2017. Using combined GRACE and GPS data to investigate the vertical crustal deformation at the northeastern margin of the Tibetan Plateau, *J. Asian Earth Sci.,* **134,** 122–129.

Zumberge, J.F., Heftin, M.B., Jefferson, D.C., Watkins, M.M. & Webb, F.H., 1997. Precise point positioning for the efficient and robust analysis of GPS data from large networks, *J. geophys. Res.,* **102**(B3), 5005–5017.

SUPPORTING INFORMATION

Supplementary data are available at *GJI* online.

Figure S1. An example of a $1^\circ \times 1^\circ$ loading calculation on a PREM earth structure. The maximum vertical deformation due to the load is several times larger than the maximum horizontal deformation.

Figure S2. Average monthly precipitation in Myanmar and Bangladesh (World Bank Group Climate Change Knowledge Portal, 2010).

Figure S3. Vertical GNSS time-series at the MIBB network, corrected for hydrological loading using each of the models explored in this paper.

Figure S4. Map of the BanglaPIRE GNSS network.

Figure S5. Vertical data at the BanglaPIRE GNSS stations showing the corrected GNSS time-series after applying a GRACE-based hydrological loading model.

Figure S6. Phasor diagram for the raw GNSS time-series before correction of non-tidal atmospheric and non-tidal ocean loading. The orange vectors are the phasors for the applied non-tidal ocean and atmosphere correction. The ocean and atmosphere loading is small and has peak uplift around July, which is consistent with a low-pressure system at the time of the monsoon.

Figure S7. Estimated phase and amplitude of horizontal seasonal oscillations in the GNSS data (black) and the GRACE models (orange).

Figure S8. The amplitude difference between LSDM and GLDAS model predictions at each station in the MIBB network. The differences between these models is hypothesized to be the loading component from rivers and lakes. The scale bar is the same as Fig. 6(a).

Figure S9. Diffusion curves for a sudden influx of surface water diffusing into the subsurface. D is the hydraulic diffusivity. The normalized flux on the *y*-axis is unitless. Hydraulic diffusivities of this range are consistent with sandstone, basalt, chalk, and karst and inconsistent with granite, marble and clay (Barbour & Wyatt 2014). In a time period of 15–30 d, water could reach a subsurface aquifer at several kilometres' depth but could not move significant distances laterally.

Table S1. Blacklist of unused GNSS stations for hydrological loading analysis.

Table S2. Amplitude, phase and velocity results for various models and the GNSS observations from MIBB and BanglaPIRE stations (included as separate text file).